BLIND DECONVOLUTION OF 3D DATA IN WIDE FIELD FLUORESCENCE MICROSCOPY

Ferréol Soulez[1], *Loïc Denis*[2,3], *Yves Tourneur*[1], *Éric Thiébaut*[2]

[1]Centre Commun de Quantimetrie – Université Lyon 1 – 8 avenue Rockefeller, 69373 Lyon cedex 08, France
ferreol.soulez@univ-lyon1.fr

[2]Centre de Recherche Astrophysique de Lyon – CNRS-UMR 5574 – Université Lyon 1 – ENS Lyon – avenue Charles André, 69561 Saint-Genis Laval cedex, France.

[3] Laboratoire Hubert Curien – CNRS UMR 5516 – Université Jean Monnet – 18 rue B. Lauras, 42000 St-Étienne, France

ABSTRACT

In this paper we propose a blind deconvolution algorithm for wide field fluorescence microscopy. The 3D PSF is modeled after a parametrized pupil function. The PSF parameters are estimated jointly with the object in a *maximum a posteriori* framework. We illustrate the performances of our algorithm on experimental data and show significant resolution improvement notably along the depth. Quantitative measurements on images of calibration beads demonstrate the benefits of blind deconvolution both in terms of contrast and resolution compared to non-blind deconvolution using a theoretical PSF.

Index Terms— blind deconvolution, wide field fluorescence microscopy, image restoration, inverses problems

1. INTRODUCTION

Using fluorescent dyes to identify specific cellular structures, the wide field fluorescence microscopy (WFFM) is a widely spread imaging modality in biology. It consists on imaging at its emission wavelength a cellular structure marked by fluorescent dye excited by uniform illumination. On the resulting 2D image, structures are more or less defocalized according to their distance to the focal plane. Moving this focal plane through the sample produces a 3D representation of the object. WFFM however suffers from a very coarse axial resolution compared to the lateral resolution. This blurring of the data $\boldsymbol{y}$ can be modeled by a 3D convolution between a point spread function (PSF) $\boldsymbol{h}$ and the observed 3D object $\boldsymbol{x}$:

$$\boldsymbol{y} = \boldsymbol{h} * \boldsymbol{x} + \boldsymbol{n}\,, \tag{1}$$

where $\boldsymbol{n}$ accounts for the noise. The resolution of the setup is given by the shape of the 3D PSF. To improve depth resolution, one can either change the imaging setup (*e.g.*, using confocal or two-photon microscopy) or enhance WFFM 3D data with a deconvolution algorithm ([1, 2] and references therein). Most deconvolution algorithms use the theoretical diffraction-limited PSF or a more realistic experimental PSF measured using calibration beads. Blind deconvolution algorithms bypass the problem of PSF calibration by simultaneously estimating the PSF and the object. Few blind deconvolution algorithms have been proposed for WFFM, the most notable being parametric blind deconvolution (PBD)[3], AIDA[4, 5] and the method proposed by Kenig[6] where the PSF is constrained to lie in a (previously learned) subspace.

The proposed method is closely related to PBD[3] method as we model a PSF as a function of a parametrized pupil function. The main differences are (i) the use of a much more robust MAP framework instead of maximum likelihood and (ii) the parametrization of the PSF that enforces its normalization and can model non-symmetric PSF.

This work has been supported by project MiTiV funded by the French National Research Agency (ANR DEFI 09-EMER-008-01).

2. MAP FRAMEWORK

In blind deconvolution both object $\boldsymbol{x}$ and PSF $\boldsymbol{h}$ are derived from the same measurements $\boldsymbol{y}$. We consider *maximum a posteriori* estimates $\{\boldsymbol{x}^+, \boldsymbol{h}^+\}$ obtained by minimizing cost function $f(\boldsymbol{x}, \boldsymbol{h})$:

$$\{\boldsymbol{x}^+, \boldsymbol{h}^+\} = \underset{\boldsymbol{x}\in\mathbb{X},\boldsymbol{h}\in\mathbb{H}}{\arg\min}\, \mathcal{J}(\boldsymbol{x}, \boldsymbol{h})\,, \tag{2}$$

$$\mathcal{J}(\boldsymbol{x}, \boldsymbol{h}) = \mathcal{J}_{\mathsf{data}}(\boldsymbol{x}, \boldsymbol{h}) + \mu\, \mathcal{J}_{\mathsf{prior}}(\boldsymbol{x})\,, \tag{3}$$

with $\mathcal{J}_{\mathsf{data}}(\boldsymbol{x}, \boldsymbol{h})$ the neg-loglikelihood, $\mathcal{J}_{\mathsf{prior}}(\boldsymbol{x})$ a regularizing prior and μ a hyper-parameter. Prior knowledge on the PSF is implicitly enforced through PSF parametrization. Regularization $\mathcal{J}_{\mathsf{prior}}$ is thus applied only to object $\boldsymbol{x}$.

2.1. Data-fitting term

Under Gaussian noise assumption, the neg-loglikelihood reads:

$$\mathcal{J}_{\mathsf{data}}(\boldsymbol{x}, \boldsymbol{h}) = (\boldsymbol{y} - \boldsymbol{h} * \boldsymbol{x})^\top \cdot \mathbf{C}_{\mathrm{noise}}^{-1} \cdot (\boldsymbol{y} - \boldsymbol{h} * \boldsymbol{x})\,, \tag{4}$$

where $\mathbf{C}_{\mathrm{noise}}$ is the noise covariance matrix and is diagonal if noise is uncorrelated:

$$\mathcal{J}_{\mathsf{data}}(\boldsymbol{x}, \boldsymbol{h}) = \sum_k w_k \left[(\boldsymbol{h} * \boldsymbol{x})_k - y_k\right]^2, \tag{5}$$

where w_k is the inverse of the noise variance at pixel k. This model can cope with non-stationary noise and can be used to express confidence on measurements on each pixel of the data. Thus it can deal with unmeasured pixels (due to saturation, borders…) by setting $w_k = 0$ for such pixels. Furthermore, except for very low detector noise, this formulation can account for mixed Poisson + Gaussian noise by approximating it as a non-stationary uncorrelated Gaussian noise [5]:

$$w_k \overset{\text{def}}{=} \begin{cases} \left(\gamma \max(y_k, 0) + \sigma_k^2\right)^{-1} & \text{if } y_k \text{ is measured,} \\ 0 & \text{otherwise,} \end{cases} \tag{6}$$

where γ is the quantization factor of the detector and σ_k^2 is the variance of other approximately Gaussian noises (*e.g.*, read-out noise) at pixel k.

2.2. Object regularization term

As most observed objects are smooth with few sharp structures (*e.g.*, edges and spikes), we use as regularizing prior a hyperbolic version of the classical 3D total variation[7]:

$$\mathcal{J}_{\mathsf{prior}}(\boldsymbol{x}) = \sum_k \sqrt{\|\nabla x_k\|_2^2 + \epsilon^2}\,. \tag{7}$$

Parameter $\epsilon > 0$ ensures differentiability of $\mathcal{J}_{\mathsf{prior}}$ at 0. When ϵ value is close to the quantization level, this function smooths out non-significant differences between adjacent pixels. In addition, since only intensities are measured, we constrain object $\boldsymbol{x}$ to be positive valued.

3. PSF PARAMETRIZATION

An abundant literature discusses PSF modeling for fluorescence microscopy. In the present work, we chose a monochromatic scalar model that defines the 3D PSF h from pupil function p. This pupil function is the in-focus point source wavefront phase and modulus at the exit pupil of the objective. To reduce the number of degrees of freedom of our model, the pupil function is parametrized by a limited number of modes.

3D PSF $h(x, y, z)$ is defined as the squared magnitude of complex-valued amplitude PSF $\bar{h}(x, y, z)$:

$$h(x, y, z) = \left|\bar{h}(x, y, z)\right|^2 . \tag{8}$$

Complex-valued PSF $\bar{\boldsymbol{h}}$ is, in turn, defined as the 3D Fourier transform of the complex-valued amplitude optical transfer function (OTF). This OTF is non-zero only on a spherical cap of radius n_{i}/λ limited by the aperture angle. It can thus be fully described by a 2D function: pupil function $p(\kappa_x, \kappa_y)$ which is non-zero on the disk defined by $\sqrt{\kappa_1^2 + \kappa_2^2} \leq \mathrm{NA}/\lambda$. 3D PSF $h(x, y, z)$ is then related to pupil function p through:

$$h(x, y, z) = \left| \iint p(\kappa_x, \kappa_y)\, \exp\left(2\,\mathrm{i}\,\pi\, z\, d(\kappa_x, \kappa_y)\right) \ldots \right.$$
$$\left. \exp\left(2\,\mathrm{i}\,\pi\,(\kappa_x\, x + \kappa_y\, y)\right)\, \mathrm{d}\kappa_x \mathrm{d}\kappa_y \right|^2 , \tag{9}$$

with $d(\kappa_x, \kappa_y) = \sqrt{(n_{\mathsf{i}}/\lambda)^2 - (\kappa_x + \kappa_y)^2}$ the defocus[8], n_{i} the refractive index of the immersion medium and λ the emission wavelength of the fluorophore. The defocus and the 2D complex pupil function $p(\kappa_x, \kappa_y)$ describe the properties of the optical system.

As noted by Hanser[9], the support of $p(\kappa_x, \kappa_y)$ is a disk thus Zernike polynomials Z_n provide a suitable basis to express both modulus $\rho(\kappa_x, \kappa_y)$ and phase $\phi(\kappa_x, \kappa_y)$ of pupil function p:

$$\rho(\kappa_x, \kappa_y) = \sum\nolimits_n \beta_n Z_n(\kappa_x, \kappa_y)\,, \tag{10}$$

$$\phi(\kappa_x, \kappa_y) = \sum\nolimits_n \alpha_n Z_n(\kappa_x, \kappa_y)\,. \tag{11}$$

As phase piston has no effect on the resulting PSF we set $\alpha_0 = 0$. Similarly, we cancel the tip-tilt parameters ($\alpha_1 = \alpha_2 = 0$) to keep the PSF laterally centered (this fixes the position degeneracy common with blind deconvolution problems). PSF normalization (i.e., energy conservation) can be expressed as an ℓ_1 norm constraint $\|h\|_1 = 1$, or equivalently as an ℓ_2 constraint on the complex-valued PSF $\|\bar{h}\|_2 = 1$. This latter ℓ_2 constraint can further be written as an ℓ_2 constraint in Zernike orthonormal basis: $\|\beta\|_2 = 1$. By selecting only purely radial Zernike polynomials, one can easily constrain the axial symmetry of the PSF. This relatively simple PSF model offers a flexible parametrization that requires only the knowledge of the wavelength λ, the numerical aperture NA and the refractive index of the immersion medium n_{i}.

4. BLIND DECONVOLUTION ALGORITHM

To solve the blind deconvolution, we have to find the optimal parameters $\{\boldsymbol{x}^+, \boldsymbol{\alpha}^+, \boldsymbol{\beta}^+\}$ that minimizes the cost function $\mathcal{J}(\boldsymbol{x}, \boldsymbol{h}(\boldsymbol{\alpha}, \boldsymbol{\beta}))$. A simple way to do this is to use continuous optimization techniques. Due to non-linearity of this cost function and as these parameters have different physical meanings, the simultaneous estimation of parameters of both the object $\boldsymbol{x}$ and the PSF $h(\boldsymbol{\alpha}, \boldsymbol{\beta})$ is known to very badly conditioned. This slows down convergence of optimization algorithm. For that reason, as it is classically done[10], we use an alternating minimization scheme to minimize the criterion $\mathcal{J}(\boldsymbol{x}, h(\boldsymbol{\alpha}, \boldsymbol{\beta}))$. The algorithm is thus:

1. $t = 0$, define the initial PSF $\boldsymbol{h}^{(0)}$ as the theoretical diffraction limited PSF of the microscope *i.e.*, $\boldsymbol{\alpha}^{(0)} = \mathbf{0}$, $\boldsymbol{\beta}^{(0)} = \mathbf{0}$.
2. $t = t + 1$, estimation of the optimal non-negative object $\boldsymbol{x}^{(t)}$ according to given PSF $\boldsymbol{h}^{(t-1)}$:

$$\boldsymbol{x}^{(t)} \approx \underset{\boldsymbol{x}\geq 0}{\arg\min} \left(\mathcal{J}_{\mathsf{data}}(\boldsymbol{x}, \boldsymbol{h}^{(t-1)}) + \mu\, \mathcal{J}_{\mathsf{prior}}(\boldsymbol{x}) \right) . \tag{12}$$

3. Improvement of the phase parameters $\boldsymbol{\alpha}^{(t)}$ given the other model parameters that minimize:

$$\boldsymbol{\alpha}^{(t)} = \underset{\boldsymbol{\alpha}}{\arg\min}\, \mathcal{J}_{\mathsf{data}} \left(\boldsymbol{x}^{(t)}, \boldsymbol{h}(\boldsymbol{\alpha}, \boldsymbol{\beta}^{(t-1)}) \right) . \tag{13}$$

4. Improvement of the modulus parameters $\boldsymbol{\beta}^{(t)}$ given the other model parameters that minimize:

$$\boldsymbol{\beta}^{(t)} \approx \underset{\|\boldsymbol{\beta}\|_2^2 = 1}{\arg\min}\, \mathcal{J}_{\mathsf{data}} \left(\boldsymbol{x}^{(t)}, \boldsymbol{h}(\boldsymbol{\alpha}^{(t)}, \boldsymbol{\beta}) \right) , \tag{14}$$

5. Go to step 2 until convergence.

Each step involves minimization of a criterion with respect to a large number of variables. To that end, we used VMLM-B algorithm [11] which can account for bound constraints on the parameters to enforce object positivity. This algorithm has proved its effectiveness for image reconstruction and only requires the computation of the cost function and its gradient. The memory requirement is a few times the size of the problem. In each step, we do not exactly solve the minimization defined in Eq. (12), Eq. (13) and Eq. (14) but only execute few iterations (about 10) of each inner optimization.

5. RESULTS

We processed the dataset[1] used by Griffa *et al.* in [14, 12] for comparative study of available deconvolution softwares. That study only considers "non-blind" deconvolution with theoretical PSF and we used it to evaluate the advantages of using a blind deconvolution technique compared to state of the art available "non blind" deconvolution methods.

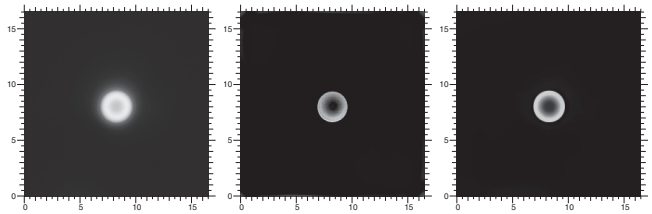
[1] the dataset can be found at `http://bigwww.epfl.ch/deconvolution`

parameters	data	Hyugens	AutoDeblur	Deconvolution Lab	proposed method non-blind	proposed method blind
transversal FWHM (in nm)	2867	2709	2709	2664	2736	2783
axial FWHM	4760	4000	4640	4160	3054	2977
Relative contrast	18 %	53 %	78 %	68 %	84 %	88 %

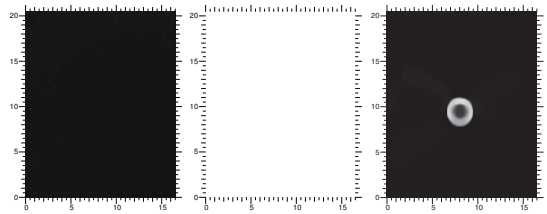
Table 1. Performance of 3 state-of-the-art deconvolution methods as reported by Griffa [12] compared to the proposed method (both blind and non-blind). Hyugens and AutoDeblur are commercial softwares and Deconvolution Lab is an imageJ plugin implementing [13].

5.1. Calibration bead

The first dataset is an observation of an InSpeck green fluorescent bead with a known diameter (2.5μm) on a Olympus Cell R microscope with a $\times 63$, 1.4 NA oil objective. The data cube is composed of $256 \times 256 \times 128$ voxels of size $64.5 \times 64.5 \times 160\,\mathrm{nm}^3$. During the first step of the algorithm, the solution of Eq. (12) is a "non-blind" deconvolution with a theoretical PSF (no aberration). On this solution, plotted in Fig. 1(b) and Fig. 1(e), the transversal resolution improvement is quite important but, in the axial section, we can notice artifacts caused by PSF mismatches. The result of our blind deconvolution algorithm (hyper-parameter set to $\mu = 10^{-3}$) is shown on Fig. 1(c) and Fig. 1(f). These figures illustrate the resolution improvement especially in the axial section with almost no artifact.



(a) XY section of original data (b) XY section of deconvolved data (c) XY section of blindly deconvolved data



(d) XZ section of original data (e) XZ section of deconvolved data (f) XY section of blindly deconvolved data

Fig. 1. Sections of observed and restored images of an InSpeck green fluorescent bead of diameter 2.5 μm. Axis are in μm

Both theoretical and estimated PSF are shown on Fig. 2. The estimated PSF is representative of wide field fluorescence microscopy. Although the in-focus axial sections of both PSF are similar, there are strong differences between axial sections. Unlike the theoretical PSF, the estimated PSF is not symmetric with respect to the plane ($z = 0$). This is well explained by a mismatch between the refractive indices of the immersion oil and the mounting medium.

To perform quantitative evaluation, Griffa *et al.* [12] proposed three criteria: the size of the bead given by the lateral and the axial full width at half maximum (FWHM) and the relative contrast between the center of the bead and the maximum of its radial profile. We present in Tab. 1, the values of these criteria given by [12] together with the values obtained with our method. We can notice that in its non-blind form (*i.e.* step 2 only), the proposed 3D-TV is competitive with the state of the art. As it tends to smooth the object, TV regularization may lead to an over-estimation of the diameter of the bead (its nominal width is $2500\,\mathrm{nm}$). However the axial FWHM and the relative contrast shows the improvements given by our blind deconvolution method.

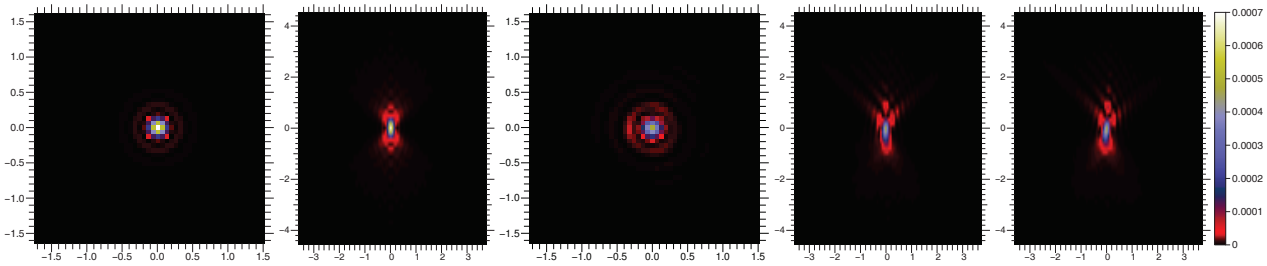
5.2. C Elegans embryo

In addition to this quantitative evaluation on a calibration bead, we processeded the biological sample used by Griffa *et al.* in their study. It is an observation of a C. Elegans embryo containing DAPI, FITC and CY3 stainings with the same microscope and objective than in previous section. The data cube is composed of $672 \times 712 \times 104$ voxels of size $64.5 \times 64.5 \times 200\,\mathrm{nm}^3$ in three spectral channels. The DAPI (blue $477\mathrm{nm}$) stains chromosomes in the nuclei, the FITC (green $542\mathrm{nm}$) the microtubule filaments and CY3 (red $654\mathrm{nm}$) some point wise protein aggregates. We processed each channel from this dataset individually using the same hyper-parameter for each channel ($\mu = 2 \times 10^{-5}$). For each channel, the algorithm takes about 4 hours to converge using an Intel i7-975 CPU. The result of the blind deconvolution (Fig. 3) presents a significantly improved contrast without the typical haze of fluorescence wide field microscopy: the red spots are much sharper and brighter in the restoration. Furthermore, the resolution is clearly improved especially along the depth axis: the out of focus nuclei encircled in red is almost invisible in the blind deconvolution. However, as it can be seen on axial sections, the deconvolution becomes less effective as one looks deeper in the sample. This can be explained by the use of a single stationary PSF for the whole observation. Because of refractive index mismatch, it is well known that the real PSF may vary axially and even laterally.

6. CONCLUSION

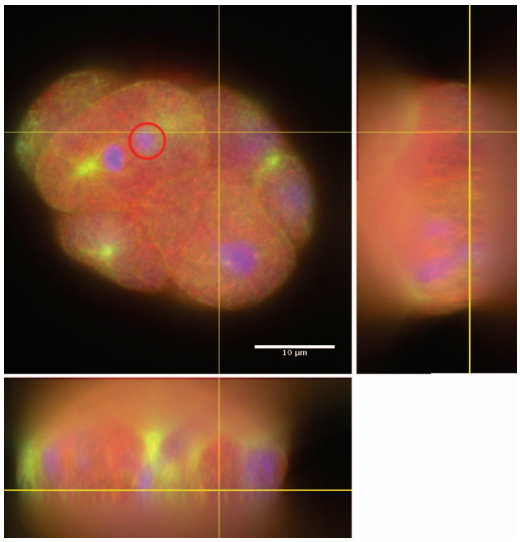
We presented a new method for blind deconvolution of WFFM data. It uses a PSF parametrization by means of decomposition of the pupil on Zernike basis. We used a continuous optimization method to iteratively estimate both PSF parameters and the object. Except from some parameters of the setup that are generally known (wavelength, numerical aperture and refractive index of the immersion medium), it requires only tuning one hyper-parameter. Results show clear improvements of both resolution and contrast.

Possible directions for future research include extension of the PSF model to more sophisticated models (*e.g.* vectorial model with pixel integration), extending this method to confocal and two photon microscopy, and introducing space-variant PSF blind-deconvolution[15].

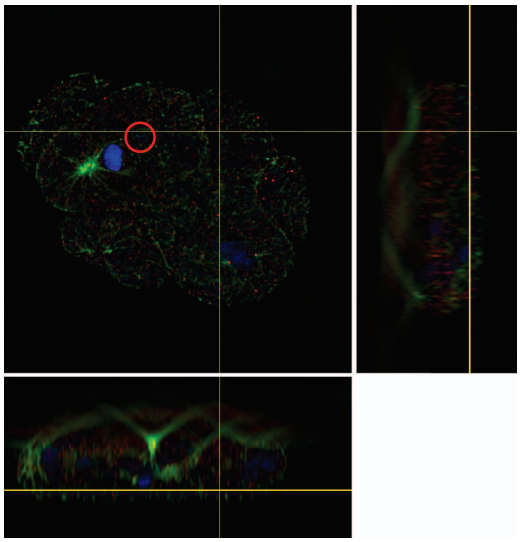


(a) XY section (b) XZ section (c) XY section (d) XZ section (e) YZ section

Fig. 2. Sections of theoretical ((a) and (b)) and estimated PSF ((c), (d) and (e)). Axis are in µm.



(a) Observation



(b) Blind deconvolution result

Fig. 3. C. Elegans embryo observation and the blind deconvolution result. Each panels are cuts in the 3D volume along the yellow lines.

7. REFERENCES

[1] J.B. Sibarita, "Deconvolution microscopy," *Microscopy Techniques*, pp. 1288–1291, 2005.

[2] P. Sarder and A. Nehorai, "Deconvolution methods for 3-d fluorescence microscopy images," *IEEE Signal Process. Mag.*, vol. 23, no. 3, pp. 32–45, 2006.

[3] J. Markham and J-A. Conchello, "Parametric blind deconvolution: a robust method for the simultaneous estimation of image and blur," *J. Opt. Soc. Am. A*, vol. 16, no. 10, pp. 2377–2391, 1999.

[4] E.F.Y. Hom, F Marchis, T.K. Lee, S. Haase, D.A. Agard, and J.W. Sedat, "Aida: an adaptive image deconvolution algorithm with application to multi-frame and three-dimensional data," *J. Opt. Soc. Am. A*, vol. 24, no. 6, pp. 1580–1600, 2007.

[5] L. Mugnier, T. Fusco, and J-M Conan, "Mistral: a myopic edge-preserving image restoration method, with application to astronomical adaptive-optics-corrected long-exposure images," *JOSA A*, vol. 21, no. 10, pp. 1841–1854, 2004.

[6] T. Kenig, Z. Kam, and A. Feuer, "Blind image deconvolution using machine learning for three-dimensional microscopy," *IEEE Trans. Pattern Anal. Mach. Intell.*, pp. 2191–2204, 2010.

[7] Rudin L.I., Osher S. and Fatemi E., "Nonlinear total variation based noise removal algorithms," *Physica D: Nonlinear Phenomena*, vol. 60, no. 1-4, pp. 259–268, 1992.

[8] P.A. Stokseth, "Properties of a defocused optical system," *JOSA*, vol. 59, no. 10, pp. 1314–1321, 1969.

[9] BM Hanser, MGL Gustafsson, DA Agard, and JW Sedat, "Phase-retrieved pupil functions in wide-field fluorescence microscopy," *Journal of microscopy*, vol. 216, no. 1, pp. 32–48, 2004.

[10] J. Besag, "On the statistical analysis of dirty pictures," *Journal of the Royal Statistical Society. Series B (Methodological)*, vol. 48, no. 3, pp. 259–302, 1986.

[11] E. Thiébaut, "Optimization issues in blind deconvolution algorithms," in *Astronomical Data Analysis II.*, Jean-Luc Starck, Ed., dec 2002, vol. 4847, pp. 174–183.

[12] A. Griffa, N. Garin, and D. Sage, "Comparison of deconvolution software in 3d microscopy. a user point of view part 2.," *G.I.T. Imaging & Microscopy*, vol. 1, pp. 41–43, 2010.

[13] C. Vonesch and M. Unser, "A fast thresholded Landweber algorithm for wavelet-regularized multidimensional deconvolution," *IEEE Trans. Image Process.*, vol. 17, no. 4, pp. 539–549, April 2008.

[14] A. Griffa, N. Garin, and D. Sage, "Comparison of deconvolution software in 3d microscopy. a user point of view part 1.," *G.I.T. Imaging & Microscopy*, vol. 1, pp. 43–45, 2010.

[15] L. Denis, E. Thiébaut, and F. Soulez, "Fast model of space-variant blurring and its application to deconvolution in astronomy," in *18th IEEE Int. Conf. on Image Proc.*, Bruxelles, France, Sept. 2011, pp. 2873–2876.